Kamal K. Taha*, Musadag M. Mustafa, Hasabo A. Mohamed Ahmed and Sarra Talab

Selenium Zinc Oxide (Se/ZnO) Nanoparticles: Synthesis, Characterization, and Photocatalytic Activity

https://doi.org/10.1515/zna-2019-0157
Received May 8, 2019; accepted August 2, 2019; previously published online September 7, 2019

Abstract: A facile synthesis of undoped and 2.0 % selenium-doped zinc oxide nanoparticles (NPs) was efficaciously accomplished through a mechanochemical route using zinc acetate dihydrate, oxalic acid, and Se powder in a solid state reaction. After calcination at 450 °C, the obtained nanostructures were probed by X-ray diffraction, where the acquired data revealed the pertinence of the wurtzite hexagonal ZnO for both undoped (ZnO) and doped (Se/ZnO) NPs and crystallite sizes of 30 and 24 nm for ZnO and Se/ZnO, respectively. The formation of the target NPs was confirmed by the scanning and transmission electron microscopy, energy-dispersive X-ray analysis, and the Fourier transformation infrared molecular vibrations data. The porosity investigations indicated 33.65 m^2/g Brunauer–Emmett–Teller surface area, 197 Å pore diameter, and 0.172 cm^3/g pore volume for the Se/ZnO NPs compared to lower values for the pristine ZnO. The band gap energies were 3.19 and 3.15 eV for ZnO and Se/ZnO as perceived from the Tauc plots of the UV-visible absorption measurements. The photodegradation of methylene blue dye under UV illumination was found to follow the pseudo–first-order kinetics with an enhanced performance by the doped samples as reflected by the higher (3.2×10^{-3} s^{-1}) rate constant relative to the undoped sample (1.7×10^{-3} s^{-1}). A photodegradation mechanism was suggested in the light of the band gap energy investigation. The obtained findings indicate the improvement of ZnO properties by doping with Se through a simplistic and inexpensive approach.

Keywords: Band Gap Structure; Organic Dye Photodegradation Mechanism; Se-Doped ZnO NPs.

***Corresponding author: Kamal K. Taha,** Department of Chemistry, College of Science, Imam Mohammad Ibn Saud Islamic University (IMSIU), Riyadh, Kingdom of Saudi Arabia; and Department of Chemistry and Industrial Chemistry, College of Applied and Industrial Sciences, Bahri University, Khartoum, Sudan, E-mail: kamaltha60@gmail.com
Musadag M. Mustafa: Sudan Academy of Science, Africa City of Technology, Khartoum, Sudan, E-mail: musadakk.mustafa@gmail.com
Hasabo A. Mohamed Ahmed: Sudan Academy of Science, Africa City of Technology, Khartoum, Sudan; and Textiles Department, College of Engineering and Technology of Industries, Sudan University of Science and Technology, Khartoum, Sudan, E-mail: profhasabo@gmail.com
Sarra Talab: Department of Chemistry, College of Science, Imam Mohammad Ibn Saud Islamic University (IMSIU), Riyadh, Kingdom of Saudi Arabia, E-mail: stalab9@gmail.com

1 Introduction

Zinc oxide is a direct wide-band-gap semiconductor having a 3.37-eV band gap in addition to a large exciton-binding energy of 60 meV [1]. These two properties make it stand as an excellent nominee for diverse applications such as optoelectronics, particularly the blue to UV light–emitting devices [2]. To improve the ZnO properties, it is usually doped with various impurities to acquire fascinating characteristics. This is achieved by developing desired properties and functions such as altering the band structure, creating defect sites, and facilitating mobility of charge carriers. Selective element doping offers a means to adjust the electrical, optical, and magnetic properties of ZnO nanowires, which are important for applications in solar cells, catalysis, and sensors [3]. Typical dopants that were employed to increase the conductivity of ZnO are group III (B, Al, In, Ga) [4], group IV (Pb, Sn), and group VI (Se) elements of the periodic table [5]. A recent study of doping of ZnO with nonmetals revealed an increase in the band gap and changes in the photoelectronic properties as compared to the undoped ZnO nanoparticles (NPs) [6]. Selenium (Se) was chosen due to its good chemical property and ease of synthesis of Se-doped ZnO [7]. Moreover, the high reduction potential of Se is thought to be a favourable condition for extracting photo-excited electrons from conduction band (CB) and hence can facilitate generation of reactive oxygen species [8]. Selenium-doped ZnO NPs were previously synthesised through mechanochemical [9], thermomechanical [8], and radiofrequency magnetron sputtering [5, 10] to improve the optical properties of ZnO. Photocatalytic reduction of

selenate (Se(VI)) and selenite (Se(IV)) ions was used to deposit nano-sized Se onto titanium dioxide (TiO_2) [11].

Wastewater industrial runoffs pose a serious menace to the biota and human health and henceforth require appropriate remediation methodology [12]. Recently, semiconductors have promptly emerged as competent heterogeneous photocatalysts for wastewater detoxification [13, 14] from such hazards. As photodegrading agents for dyes, semiconductor catalysts have greater advantages over conventional types (adsorption, flocculation, chlorination, and ozonization) such as low cost, sustainability, environmental compatibility, and the ease of performance by just irradiation with the appropriate visible and UV light [15, 16].

Herewith, we demonstrate that the synthesis of undoped and Se-doped ZnO NPs using mechanical route was achieved by adding Se powder to the reaction medium. The structural and morphological parameters describing the produced ZnO nanostructures were derived from the different techniques experimental data. The fabricated nanomaterials were used to decolourise methylene blue (MB) dye under UV illumination, and the kinetics of the process was probed.

2 Materials and Methods

2.1 Synthesis of Pristine ZnO NPs Se/ZnO NPs

To synthesise the pristine ZnO NPs, 25 mmol (5.48 g) of zinc acetate dihydrate ($Zn(CH_3COO)_2\cdots 2H_2O$) (≥98 % purity; Sigma-Aldrich, Germany) and 42 mmol (3.78 g) of oxalic acid ($H_2C_2O_4{\cdot}2H_2O$) (98 % purity; Sigma-Aldrich, Germany) were mixed and ground in an agate mortar at ambient temperature [9]. The grinding was continued until the smell of acetic acid ceased after 30 min signifying the reaction accomplishment resulting in a hydrated ZnC_2O_4 formation. Subsequently, the ZnO NPs were obtained by heating the synthesised hydrated ZnC_2O_4 in a quartz crucible at 450 °C for 30 min in a temperature-controlled furnace. To prepare Se/ZnO NPs, 0.5 mmol (0.04 g) of Se powder (≥99.9 % purity; Merck) was added to a mixture of the aforementioned zinc acetate and oxalic acid precursors, and the same procedure was followed. The as-synthesised nanostructure was washed with ethanol and oven dried at 80 °C for 6 h before annealing at 450 °C for 30 min.

2.2 Nanoparticles Characterization

The microstructure of photocatalysts was determined by X-ray diffraction (XRD) diffractometer (D8-Advance; Bruker, Germany) using Cu-Kα radiation, $\lambda = 0.15406$ nm; accelerating voltage is 40 kV and 20–80° as scanning angle range. The morphology of the prepared samples was probed with a field emission scanning electron microscopy (SEM, JEM-6700F; JEOL, Tokyo, Japan) and a transmission electron microscopy (TEM, JEM-2100; JEOL). The samples were previously oven dried at 105 °C and coated with a thin film of Pt to provide ZnO powder surface with electrical conduction. The composition analysis of nanostructures was conducted using the energy-dispersive X-ray (EDX) spectrometer. The Brunauer–Emmett–Teller (BET) specific surface area was evaluated through N_2 adsorption–desorption isotherms. Prior to each analysis, the ZnO sample was outgassed at 250 °C for 6 h by a constant flow of helium. The porosity of the nanomaterial was obtained employing the BET equation and the t-plot method of Lippens and de Boer [17]. The molecular vibrations of the fabricated samples were studied by Fourier transform infrared spectroscopy (Nicolet 6700, Greenbay, WI, USA) in the range 4000–400 cm^{-1} with a resolution of 4 cm^{-1}. UV/Vis/NIR (Near Infrared) solid-state UV-visible (UV-vis) absorption spectra for powder samples were recorded on a Perkin-Elmer Lambda 950 UV/Vis/NIR spectrophotometer (Waltham, MA, USA), equipped with a 150-mm snap-in integrating sphere for capturing diffuse and spectral reflectance.

2.3 Photocatalytic Degradation Studies

Methylene blue dye was employed as the test contaminant for investigating photocatalytic activities of the synthesised ZnO and Se/ZnO NPs. The experiments were carried out as follows: 50 mg of the prepared catalyst was added to 100 mL MB solution (10 mg/L). Before illumination, the suspensions were magnetic stirred by in the dark for 1 h, to ensure the MB uniform adsorption onto the surface of catalyst. Thereafter, the suspension was placed in a Heber multilamp photoreactor equipped with eight low-pressure 125-W UV lamps arranged in a circular manner emitting a radiation at fixed $\lambda = 254$ nm (4.88 eV) under continuous stirring condition. Five millilitres of suspension was collected in a tube at different time intervals and then centrifuged at 6000 rpm for 7 min to remove the photocatalytic. UV-visible absorption of the supernatant was used to evaluate the photocatalytic degradation for MB dye. The percentage photocatalytic degradation was estimated using the formula [18]:

$$\text{MB}\,\% = \frac{C_0 - C_t}{C_0} \times 100 = \frac{A_0 - A_t}{A_0} \times 100 \qquad (1)$$

where C_o and C_t are the MB initial (10 mg/L) and time t concentrations, respectively, whereas the A_0 and A_t stand for the absorbance at $t = 0$ and time t, respectively.

3 Results and Discussion

3.1 X-ray Diffraction Analysis

Typical XRD patterns of ZnO and Se/ZnO NPs displayed in Figure 1 exhibit different peaks at angles 2Θ of ≈ 31.9°, 34.6°, 36.4°, 47.8°, 56.8°, 64.1°, 66.7°, 68.1°, and 69.2° corresponding to the respective reflections from the (100), (002), (101), (102), (110), (103), (200), (112), and (201) crystal planes of the hexagonal wurtzite ZnO structure (JCPDS 36-1451) but no peaks corresponding to the JCPDS 06-0362 of the Se. The concordant XRD peaks broadening with less intensity for the Se-doped NP pattern relative to those of pristine ZnO NPs is perceived. The peaks broadening might be attributed to the reduction in crystallite size, whereas the lower intensity indicates a decrease in the ZnO

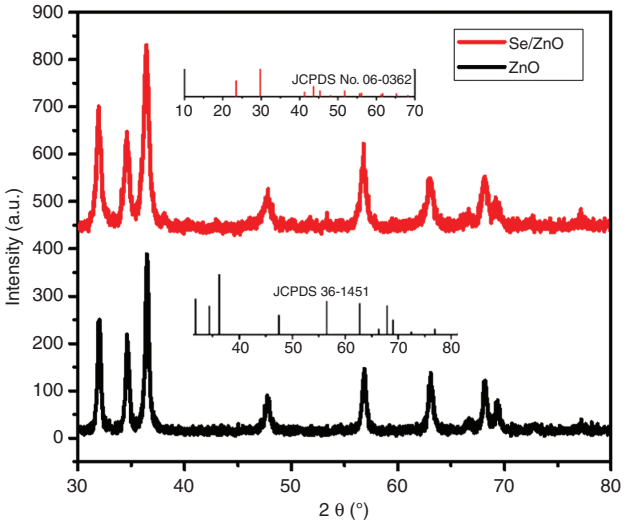

Figure 1: XRD patterns of ZnO and Se/ZnO NPs.

wurtzite phase crystallinity as a result of Se confinement [19]. The smaller crystallite size of Se/ZnO NPs could be attributed to the Se^{+4} (0.050 nm) [20] replacement of Zn^{+2} (0.074 nm) in the ZnO matrix. This reduction in crystallite size is in consistence with previous reports of the synthesis of Se-doped ZnO NPs using Se powder precursor in a solid state reaction [8] (Tab. 1).

The lattice parameters a and c were obtained using the following formula [19]:

$$a = \frac{\lambda}{\sqrt{3}\sin\theta\,101}, c = \frac{\lambda}{\sin\theta\,002} \tag{2}$$

The crystallite sizes (D) of the ZnO NPs were calculated using Scherer equation [21]

$$D = \frac{k\lambda}{\beta_{hkl}\cos\theta} \tag{3}$$

where λ is the wavelength of the incident X-ray (1.5406 Å) for Cu Kα, k is a constant equal to 0.90 [22], β_{hkl} is the peak width at half-maximum intensity (FWHM), and θ is the peak position. The (101) plane (the strongest) was selected to estimate the crystallite size. The lattice parameters a and c and the c/a ratio for the two samples as given in Table 1 are identical to those previously reported [22], for ZnO NPs prepared by standard methods. Moreover, the broadening of the Se/ZnO XRD peaks indicates the production of smaller size nanocrystallites as confirmed by the Scherer equation calculations [19].

The d spacing was calculated using Bragg's law 4, as well as the formula that relates it to the lattice constants 5:

$$d = \frac{\lambda}{2\sin\theta} \tag{4}$$

$$\frac{1}{d^2_{(hkl)}} = \frac{4}{3}\left(\frac{h^2 + hk + k^2}{a^2}\right) + \frac{L^2}{c^2} \tag{5}$$

The d_{hkl} for the different samples, calculated by both Bragg and theoretical equations, showed great similarity (Tab. 2). The microstrain (ε) is given by the formula:

$$\varepsilon = \frac{\beta}{4\tan\theta} \tag{6}$$

and dislocation density (δ), which indicate the amount of defects is defined as the length of dislocation line per unit volume of crystal, was calculated via relation [23]:

$$\delta = \frac{l}{D^2} \tag{7}$$

The Zn–O bond length (L) was given by the expression [24]:

$$L = \sqrt{\left(\frac{a^2}{3}\right) + c^2\left(\frac{1}{2} - \mu\right)^2} \tag{8}$$

where μ is the measure of an atom displacement to the neighbouring one along the "c" axis. The value of μ was calculated by the following equation:

$$\mu = \frac{a^2}{3c^2} + 0.25 \tag{9}$$

Table 1: The lattice constant values for the different samples.

Sample	2θ°	$\beta_{(FWHM)}$	D(nm)	a(Å)	c(Å)	c/a
ZnO	36.4840	0.2782	30.067	3.2328	5.1778	1.6016
Se/ZnO	36.4092	0.3535	23.657	3.2309	5.1807	1.6035

Table 2: The lattice constant value for the samples.

Sample	ε (10^{-3})	δ (10^{-3}) (nm^2)	d* (Å)	d** (Å)	Reduction	L(Å)	μ	V (Å)^3	σ (GPa)
ZnO	3.683	1.1062	2.4636	2.4627	0.4999 %	1.9674	0.3799	46.862	−1.2666
Se/ZnO	4.691	1.7868	2.4650	2.4619	0.4997 %	1.9666	0.3796	46.833	−1.1368

*d**, Bragg; *d***, calculated.

The unit cell volume was calculated as follows $V = 0.866a^2c$ [25]. The stress σ (GPa) in the crystallite's planes was determined using the formula, $\sigma = -233\left(\frac{c_{bulk}-c}{c_{bulk}}\right)$, where c is the lattice parameter crystallite's planes calculated from XRD analysis, and c_{bulk} is the strain-free lattice parameter of ZnO (5.2061 Å). Those calculations are summarised in the Table 3. The μ parameter is changed with c/a ratio in a way to maintain the tetrahedral dimension due to the angle distortion. From Table 3, it can be seen that μ differs with c/a ratio. On the other hand, the L value obtained is almost equal to the 1.9767 Å value reported by Seetawan et al. [24]. It can be observed that due to the volume shrinkage of crystallite size the bond length and the lattice volume of ZnO are more than those of Se/ZnO NPs [26]. The smaller dislocation density for pristine ZnO (1.1062×10^{-3} nm^2) than Se/ZnO NPs (1.7868×10^{-3} nm^2) is an indication of the higher crystallinity of the ZnO [27] as manifested by the sharp XRD peaks (Fig. 1), as well as the increased defects in the Se/ZnO crystal structure [28]. On the other hand, the microstrain is greater for Se/ZnO, confirming the crystallite size reduction [29].

3.2 Williamson–Hall Models

According to the Williamson–Hall (W-H) method [19], strain and crystallite size greatly influence diffraction lines broadening [30]. The three models, i.e. uniform deformation model (UDM), uniform stress deformation model (USDM), and uniform deformation energy density model (UDEDM) were considered to evaluate the homogeneity of strain, stress, or strain energy density [31]:

$$\text{UDM: } \beta_{hkl}\cos\theta_{hkl} = \frac{k\lambda}{D} + 4\varepsilon\sin\theta_{hkl} \tag{10}$$

$$\text{USDM: } \beta_{hkl}\cos\theta_{hkl} = \frac{k\lambda}{D} + \frac{4\sigma\sin\theta_{hkl}}{Y_{hkl}} \tag{11}$$

$$\text{UDEDM : } \beta_{hkl}\cos\theta_{hkl} = \left(\frac{k\lambda}{D}\right) + \left(4\sin\theta_{hkl}\left(\frac{2u_{ed}}{Y_{hkl}}\right)^{0.5}\right) \tag{12}$$

The strain was derived from the linear plot of $\beta_{hkl}\cos\theta_{hkl}$ versus $4\sin\theta_{hkl}$ of 11 [32]. Uniform deformation model: According to the W-H method [19], strain and crystallite size greatly influence diffraction lines broadening [30]. In the (USDM model, Hooke's law denotes the strain in addition to a direct relation $\sigma = \varepsilon Y_{hkl}$ linking the stress (σ), anisotropic microstrain (ε), and Young's modulus (Y_{hkl}). For hexagonal ZnO NPs, (Y_{hkl}) was given as 127 GPa [33]. From the linear plot of $\beta_{hkl}\cos\theta_{hkl}$ versus $\frac{4\sigma\sin\theta_{hkl}}{Y_{hkl}}$, σ and D were estimated from the slope and intercept, respectively, while ε is enumerated from the Young's modulus, Y_{hkl}.

In case of elastic systems that obey with Hooke's law, crystal's energy density (u_{ed}), which is interrelated to the strain by the term $u_{ed} = (\varepsilon^2 Y_{hkl})/2$ [33], was calculated from $\beta_{hkl}\cos\theta_{hkl}$ against $4\sin\theta_{hkl}\left(\frac{2u_{ed}}{Y_{hkl}}\right)^{0.5}$ plots. The stress (σ) and microstrain (ε) were obtained from (u_{ed}) and Y_{hkl}, whereas the crystallite size (D) is valued from intercept [33]. Figure 2a–c illustrate the W-H models plots, and the obtained parameters are recorded in Table 3.

The crystallite size (D) values estimated using the UDM, UDSM, and UDEDM models are virtually similar, demonstrating that the insertion of strain in the W-H method models has insignificant impact on the average (D) value. However, the average crystallite sizes estimated from Scherrer and W-H equations show slight disparity that can be ascribed to variation of size distribution averaging [19]. The entire ε and σ values determined via the three W-H models are inversely related to the crystallite size in agreement with formerly reported data [34, 35]. When comparing the data estimated by the three models, it can be perceived that there is great similarity between the parameters' values confirming the isotropic character of the nano.

3.3 FT-IR Spectra of the NPs Structures

The Fourier-Transformation Infrared (FT-IR) spectra for the two samples (Fig. 3) are drawn in in the absorption range between 417 and 3442 cm^{-1}, which represents the characteristic of the normal stretching and bending

Table 3: Parameters from SEM, Scherrer, and W-H models.

Sample	SEM (nm)	Scherrer D (nm)	W-H method								
			UDM		USDM			UDEDM			
			D (nm)	$\varepsilon \times 10^{-3}$	D (nm)	$\varepsilon \times 10^{-3}$	σ (MPa)	D (nm)	$\varepsilon \times 10^{-3}$	σ(MPa)	u_{ed} (KJm^{-3})
ZnO	40.36	30.07	37.65	1.9	31.52	0.6	76.2	32.25	0.6	9.56	0.0229
Se/ZnO	25.03	23.66	21.17	1.4	20.23	0.5	63.5	20.69	0.4	6.37	0.0102

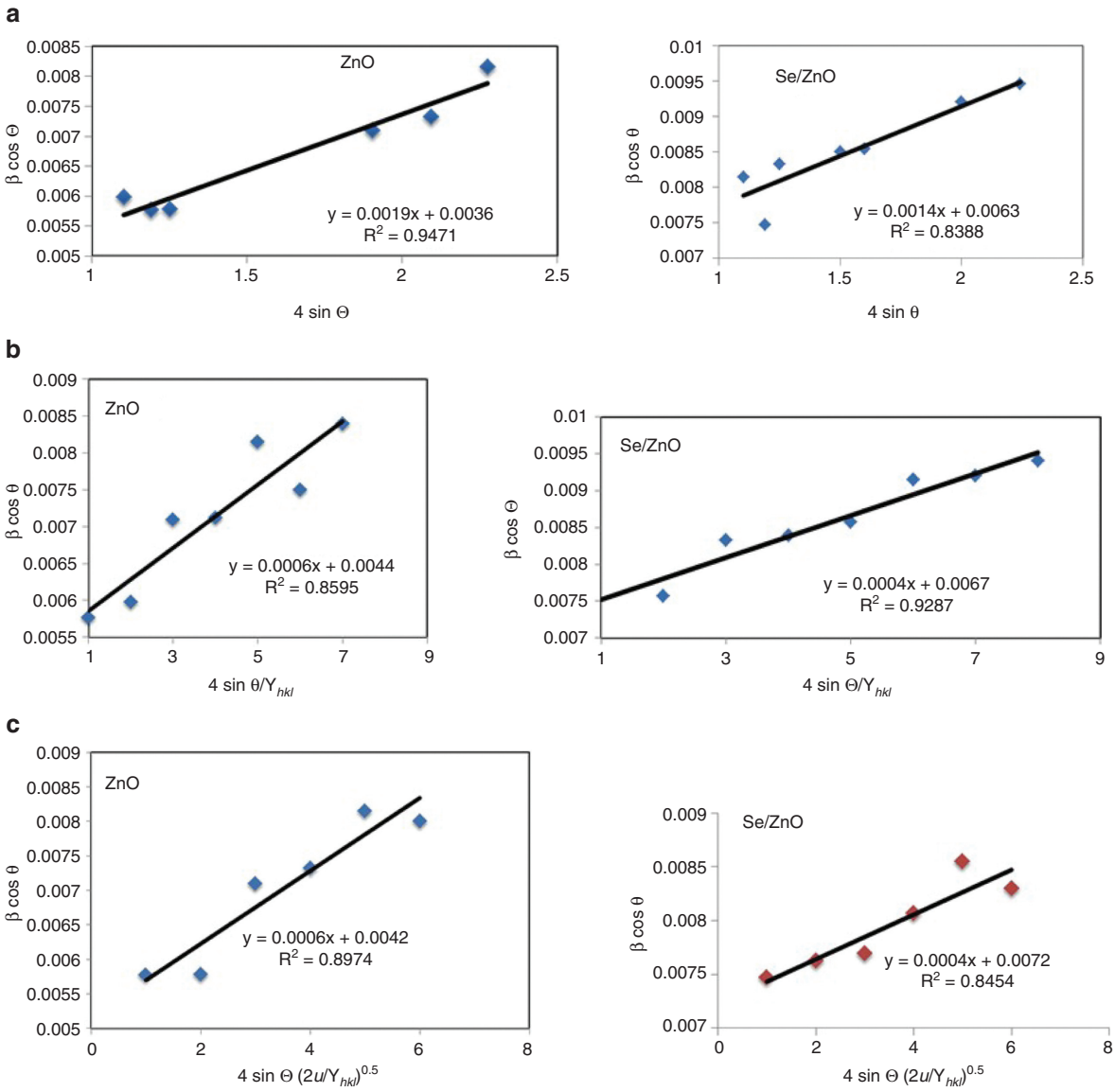

Figure 2: (a) UDM graphs for the ZnO and Se/ZnO NPs. (b) USDM graphs for the ZnO and ZnO/Se NPs. (c) UDEDM graphs for the ZnO and Se/ZnO NPs.

molecular vibrations. The presence of atmospheric CO_2 is indicated by a sharp absorption peak 2342 cm^{-1} [36]. The absorption band around 1385 cm^{-1} is assigned to the carboxyl group C=O stretching vibration, but it was shifted to 1328 cm^{-1} as a result of Se doping. A similar shift in the O–H stretching peak from 3446 to 3434 cm^{-1} is another clue for the Se doping. The data show the metal oxygen (M–O) vibrational band at the low wave number part of the IR region where the characteristic Zn-O vibrational band at 494 cm^{-1} [37] for Se/ZnO has shifted to 432 cm^{-1} as Se was incorporated into the ZnO matrix. This shift may attributed to the weakening of the bond and the subsequent low force constant [38]. This observation is consistent with the lower covalency of Zn-O due to addition of Se [39].

3.4 Morphology of the Samples

The SEM images in Figure 4 and size distribution shows that the pure ZnO NPs have a diameter range between 25.9 and 49.1 nm, while Se/ZnO was decreased to 18.1–33.4 nm in agreement with the results obtained by XRD. All pictures indicated that the samples were in the nanoscale range.

The TEM images of the zinc oxide NPs reveal the nanometric dimension of the pristine ZnO and Se/ZnO NPs. Transmission electron microscopy images of pure ZnO NPs in Figure 5 show the NPs shapes are hexagonal with average size range 22.48–30.59 nm. Furthermore, the shape of Se/ZnO has changed to spherical with a size

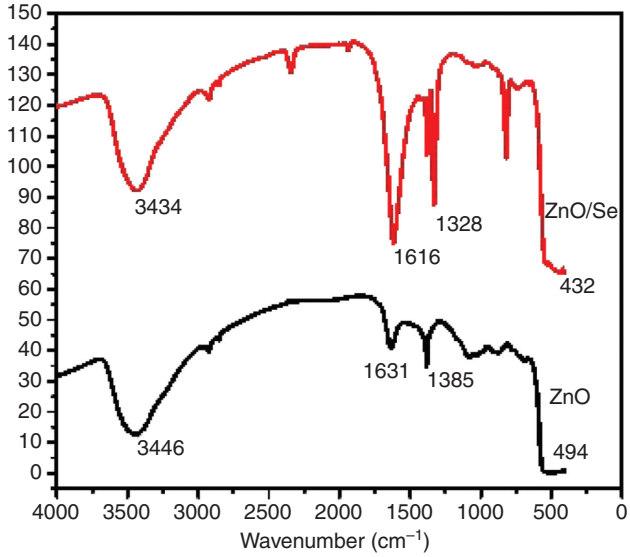

Figure 3: FT-IR spectrum of ZnO and Se/ZnO NPs.

of 7.52–11.27 nm as a result of Se addition. These results correlate well with the XRD results. The lattice *d* spacing between adjacent lattice planes in the TEM images was found to be approximately 0.255 nm for Se/ZnO NPs; this result agrees with Bragg's *d* spacing of the XRD data.

The EDX spectrum of the ZnO sample (Fig. 6a) reveals the presence of Zn and O signals with the stoichiometry of the pristine NPs. On the other hand, the doped sample shows an Se signal beside the Zn, O with a different percentage as shown in the table in Fig. 6a inset. The Se peak looks small due to the Zn Lα lines that overlap the Se Lα lines. It can be undoubtedly seen that the weight of Zn is less in the Se/ZnO sample, suggesting a possible substitution of Zn by Se [20] as indicated in the XRD pattern. Moreover, the increment in O weight in the Se/ZnO NPs may be explained by the formation of the Se-containing zinc species that has more O than the ZnO. It is interesting to observe that the 3 % increase in O is twice the 1.5 % Se ratio, which may support the Se-containing NP formation. Zinc selenite ($ZnSeO_3$), which is an intermediate of Zn and Pb calcination [40], may have been formed. According to a previous study by Korneeva and Novoselova [41], $ZnSeO_3$ melts and dissociates above 620 °C. Therefore, the less amount of Se in the formed NPs may be ascribed to the volatilisation of low melting point SeO_2 (340 °C) from the surface of Se/ZnO NPs as reported in a similar study [8].

An elemental mapping for the Se, Zn, and O were exposed as different colours to ascertain their dispersal within the NPs (Fig. 6b). A brighter zone in the elemental map describes a high content of the analogous element. The uniform colour distribution of the Se, Zn, and O provides a substantial evidence for a successful preparation of the Se-doped zinc oxide NPs

3.5 Nitrogen Adsorption BET Analysis

The N_2 absorption–desorption isotherms of the samples were measured by using the static volumetric absorption analyser. Figure 7 shows the typical nitrogen sorption isotherms of Se/ZnO and ZnO NPs. It shows the sample presents a typical IV adsorption isotherm as classified by International Union of Pure and Applied Chemistry (IUPAC) [37]. Conferring to the Kelvin equation, capillary condensation is not likely to occur when $P/P_0 < 0.5$; consequently, the adsorption hysteresis loops no longer exist as can be seen in both graphs, whereas the appearance of a pronounced hysteresis at the relative high pressure region ($P/P_0 < 0.6$) shows that the evaporation from pores is a markedly different process than condensation in the pores, which also advocates the incidence of capillary condensation within the mesopores [42]. The average diameter of the (d_{BET}) was calculated using the formula [43]:

$$d_{BET} = \frac{6000}{SSA(\mathrm{m^2/g})\rho(\mathrm{g/cm^3})} \tag{13}$$

where SSA is the specific surface area calculated using the BET isotherm, and ρ is the material density. The value was found to be 32 nm; due to the capillary agglomeration phenomenon, the isotherms increase rapidly and form a lag loop. The specific surface area of the sample was 33.6525 m^2/g calculated from BET adsorption equation. For the ZnO NPs, the BET surface area is 11.4210 m^2/g, and the (d_{BET}) is 87 nm.

Figure 7 (inset) depicts a typical Barrett-Joyner-Halenda (BJH) desorption pore size distribution curves of Se/ZnO; we can see that in most of the mesoporous with a size smaller than 500 Å (or 50 nm), the pore size of distribution estimated from the peak position is about 250 Å (or 25 nm), and possessing a relatively narrow pore size distribution, the Se/ZnO showed a relative concentrated pore distribution range from 5 to 55 nm. Based on the BJH academic model, the average pore diameter, pore volume, and pore diameter distribution of Se/ZnO are 196.934 Å, 0.1724 cm^3/g, and 25 nm, respectively. In comparison, the undoped ZnO sample showed the average pore diameter, pore volume, and pore size distribution as 120.0 Å, 0.0.0532 cm^3/g, and 18 nm, respectively. Thus, it can be concluded that the Se doping of ZnO has increased the BET surface area and porosity of the sample. The reduction in surface area of ZnO is consistent with the crystal size increment obtained from XRD and morphology data.

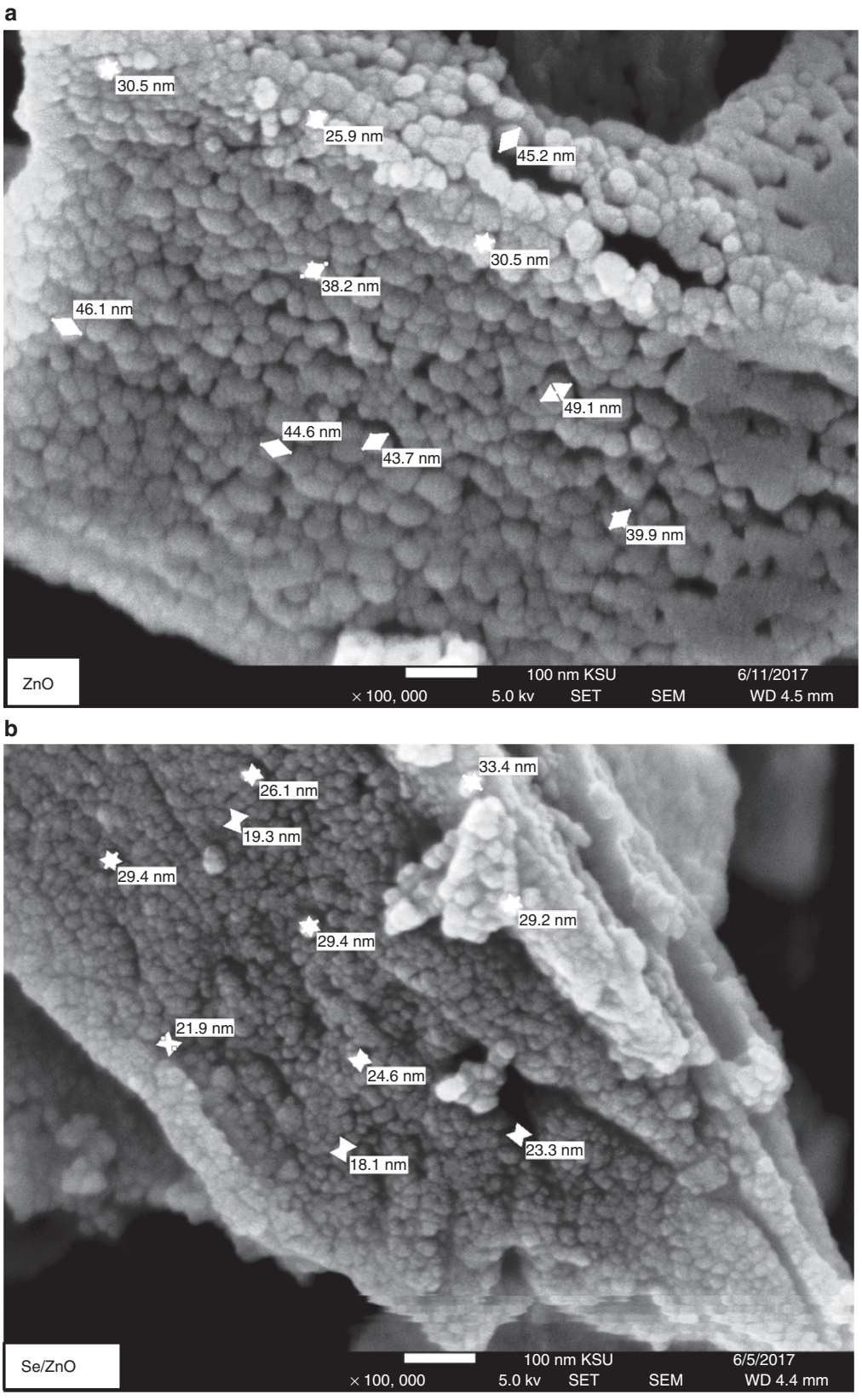

Figure 4: The SEM images of ZnO and Se/ZnO NPs.

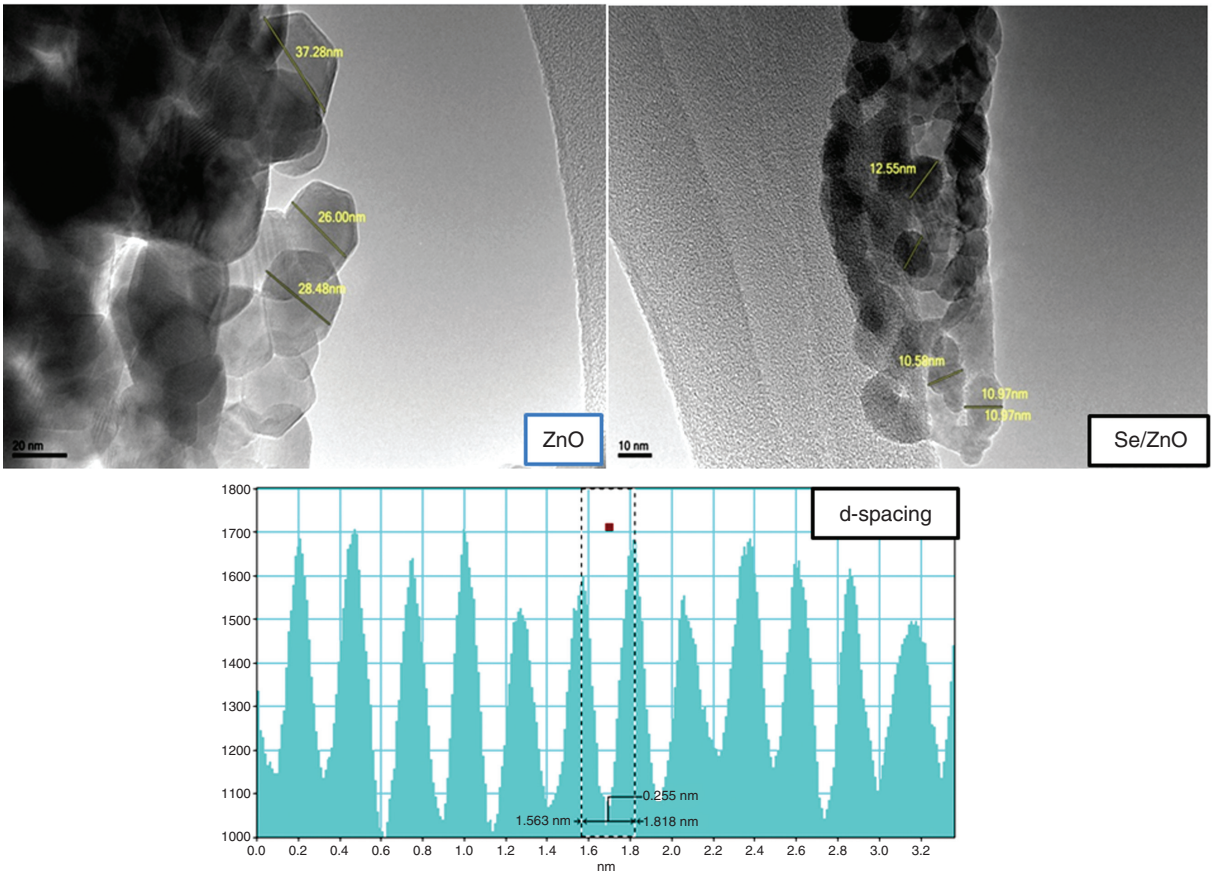

Figure 5: The TEM images of ZnO and Se/ZnO and *d* spacing.

We noticed that the size obtained from the BET, TEM, and SEM methods agrees very well with the result given by X-ray line broadening. The results of TEM, SEM observation, and BET methods further conformed and verified the relevant results obtained by XRD as mentioned above.

3.6 Thermogravimetric Analysis

The thermogravimetric analysis curve for ZnO (Fig. 8) indicates a weight loss at 100 °C due to water evaporation along with another weight loss at 200–400 °C that may be attributed to loss of organics such as CO_2 that results from the decomposition of ZnC_2O_4 to ZnO and CO_2 in addition to the water of hydration [44, 45]. The same trend is evident in the Se/ZnO samples with a more weight loss at 400 °C that may be due to the volatilisation of SeO_2 from the doped NPs as the melting point of SeO_2 is within this temperature range as reported in a similar study [8]. According to this finding, the prepared samples were calcined at 450 °C.

3.7 Optical Properties and Determination of Energy Band Gap

To explore the optical characteristics of the pure and doped ZnO nanostructures, the spectra were scanned in the 200- to 800-nm range of the electromagnetic spectrum as portrayed in Figure 9a. The UV data reveal a blue shift of the ZnO/Se absorption edge from 389 to 395 nm due to the Se loading [46]. This absorption edge shift typically denotes a change in semiconductor energy gap [47]. Phenomena such as the quantum confinement of Se in the nanoscale size regime, partial merger of Se into the ZnO host matrix, and grain boundaries formation may contribute to the spectral lines shift [48, 49]. With the incorporation of Se, the peaks are shifted to longer λ showing sturdier absorption closer to visible region than pure ZnO. The band gap energies of the samples were estimated using the Tauc equation [50]:

$$(\alpha \mathrm{hv})^{1/2} = A(\mathrm{hv} - E_g) \tag{14}$$

where the terms h, ν, α, and E_g represent Planck's constant, frequency, absorption coefficient, and band gap

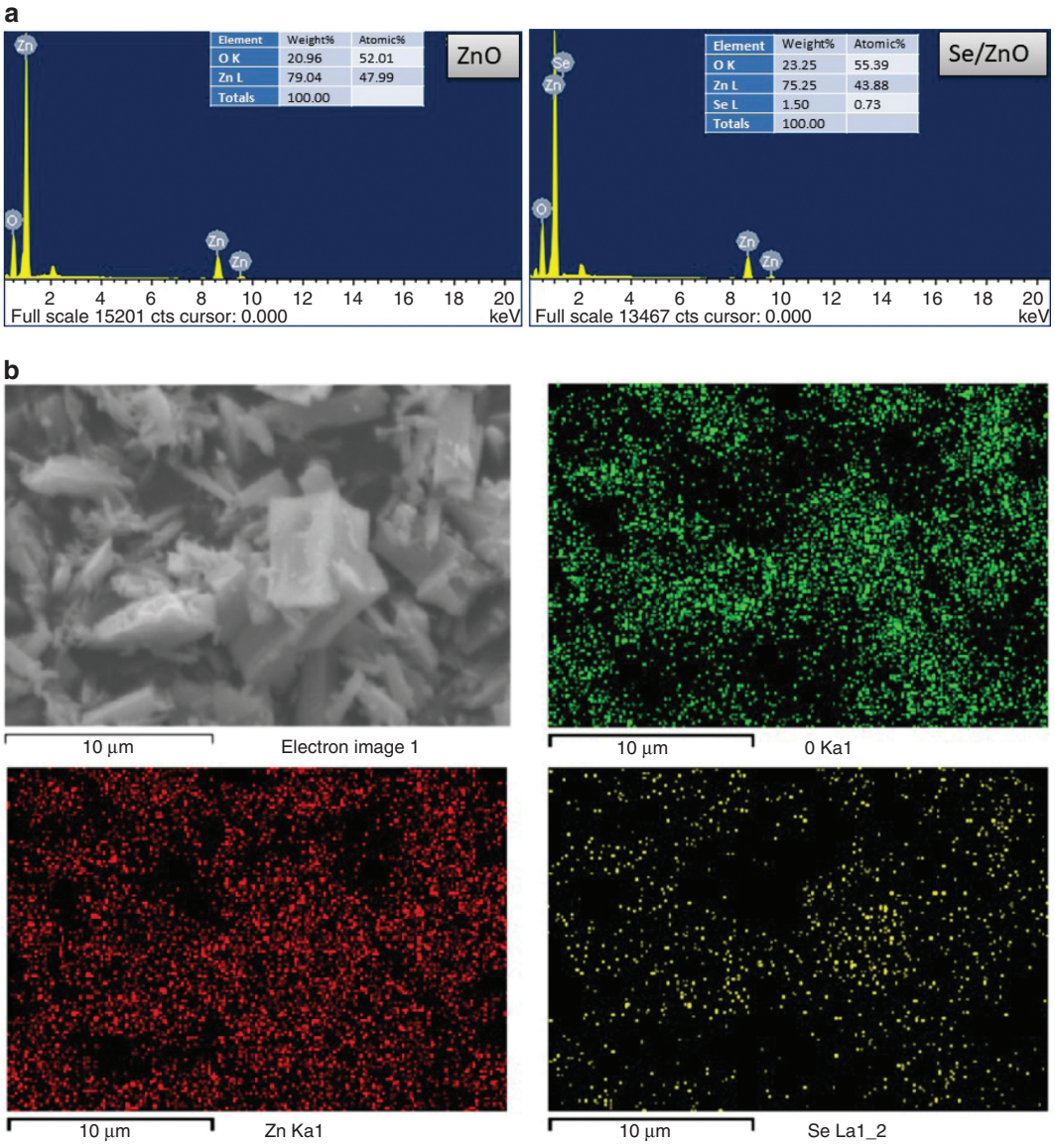

Figure 6: (a) The EDX spectrum for ZnO and Se/ZnO NPs. (b) Elemental mapping of the Se/ZnO NPs.

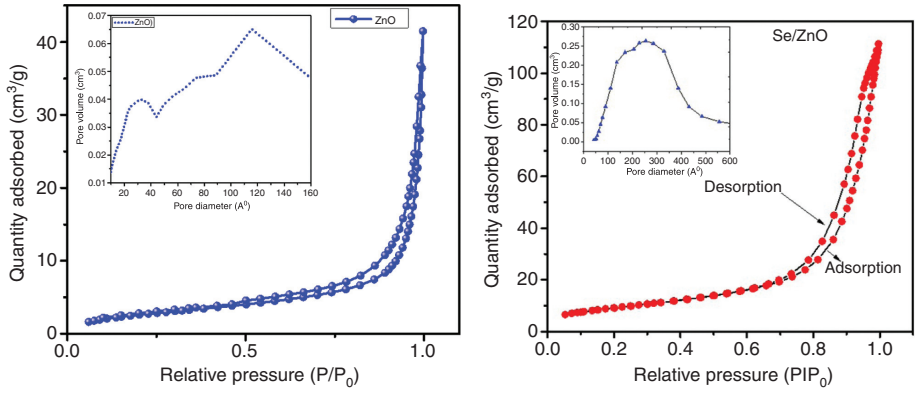

Figure 7: Nitrogen absorption–desorption isotherms and pore size distribution (inset) for ZnO and Se/ZnO.

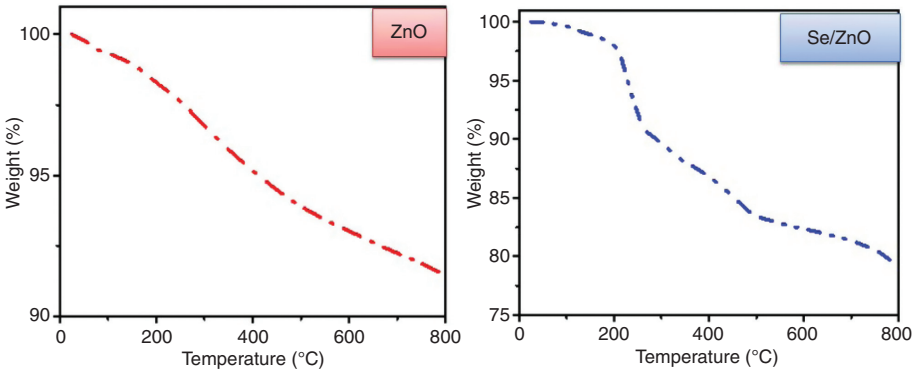

Figure 8: Thermogravimetric (TGA) analysis ZnO (a) ZnO/Se NPs.

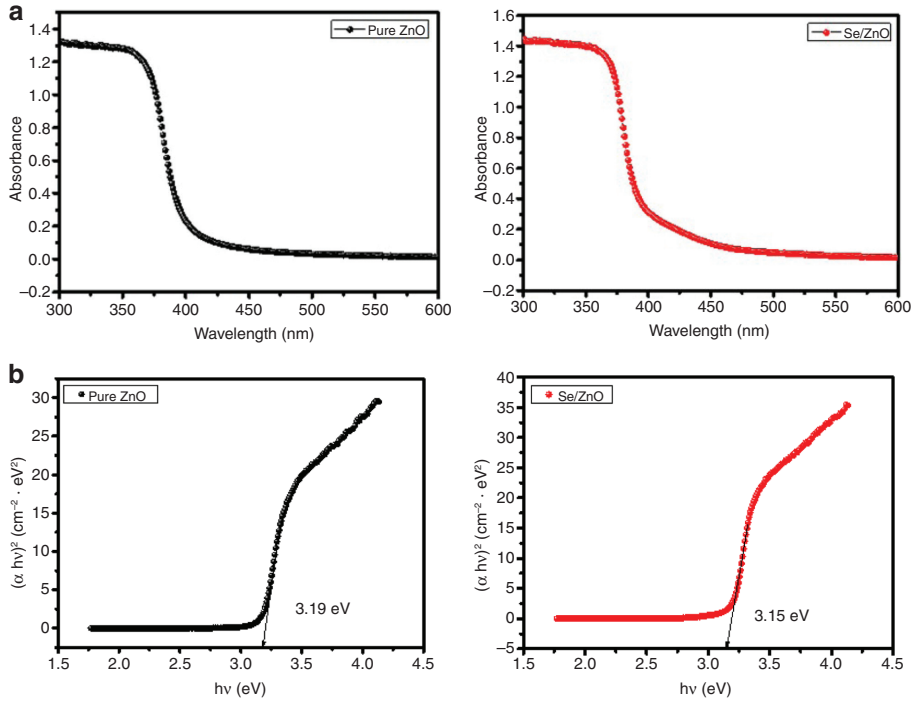

Figure 9: (a) UV-vis absorption spectra of ZnO and Se/ZnO samples. (b) $(\alpha h\nu)^2$ vs. (hv) curves of ZnO and Se/ZnO NPs.

energy, respectively. A is a proportionality constant, and n denotes the type of electron transition (for directly allowed transitions, $n = 1/2$). As can be depicted from $(Ahv)^2$ versus energy plots (Fig. 9b), the 3.19 eV energy band gap of ZnO has decreased to 3.15 eV as a result of Se doping. The presence of a single band is in contrast to the multiple valence band (VB) edge reported by Gupta and Pandey [51] for composites that may support the doping of Se in the ZnO matrix. The lower energy band gap of the pure ZnO (3.12 eV) compared to that of the bulk (3.37 eV) can be associated with the band gap narrowing commonly linked to quantum confinement effect due to size reduction to the nanoscale [49]. Similar decrease in the band gap was reported for Se-doped ZnS NPs, which was credited to structural defects such as Zn and sulphur vacancies or cations at interstitial site that form interstitial energy levels in the forbidden gap NPs [14, 52]. Other studies attributed the band gap narrowing to the O vacancy concentrations in ZnO [53]. At the 450 °C annealing temperature considered in this study, there are an increased number of O vacancies. In such situation, the impurity states are more delocalised and can overlap with the VB edge, leading to the band gap narrowing [53]. This decrease in the band gap for Se-doped ZnO NPs can also be due to structural defects corresponding to interstitial energy levels in the forbidden gap, which could be attributed to Zn vacancies and oxygen vacancies as reported in considerable doping studies [14, 52, 54].

3.8 Photodegradation Study

The photocatalytic performance of the ZnO and Se/ZnO nanostructures was probed through the photodegradation of MB as a typical organic pollutant dye. The degradation process was monitored by gauging the visible light absorbance of MB at $\lambda_{max} = 662$ [55] and different illumination time intervals under UV irradiation (Fig. 10a and b). A steady decline in absorbance is a confirmation of an improved photocatalytic capability of the prepared sample in the visible region of spectrum. The percentage photodegradation was estimated using 1 for both NPs samples. The Se/ZnO NPs exhibited higher photodegradation efficiency compared to the ZnO sample as can be observed from the histogram displayed in Figure 11. The catalytic efficiency of the prepared ZnO photocatalyst is superior to the $BaTiO_3$ NPs that showed similar results with low MB concentration of only 5 mg/L [55]. The MB photocatalytic degradation kinetics is demonstrated in Figure 12a and b, where the data were plotted for both samples in accordance with to the pseudo–first-order kinetics model:

$$\ln\left(\frac{C_0}{C_t}\right) = \ln\left(\frac{A_0}{A_t}\right) = kt \tag{15}$$

The two graphs reveal excellent compliance with the pseudo–first-order kinetics as indicated by the high regression constants (R^2) value (0.99) [56]. The rate constants as obtained from the slopes are equal to $k_1 = 3.2 \times 10^{-3}$ min^{-1} and $k_2 = 1.7 \times 10^{-3}$ min^{-1} for Se/ZnO and ZnO, respectively. The improved performance of the doped sample is reflected by the higher value of the rate constant. The higher photocatalytic activity of the Se/ZnO may be attributed to the lower band gap energy and the higher surface area that can make more dye exposed to the electrons and holes. Moreover, an impurity Se can function as a charge carrier trap, delaying the

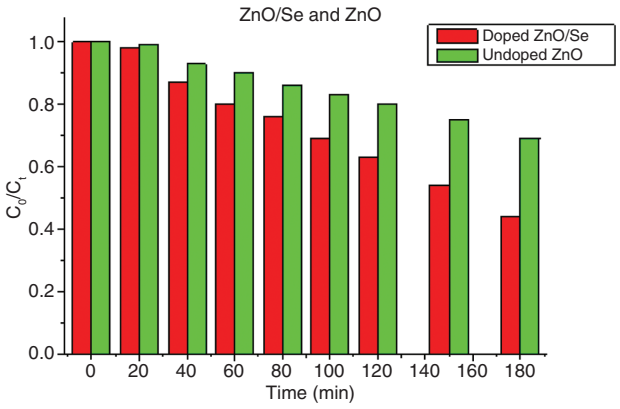

Figure 11: Time-dependent photocatalytic degradation kinetics of MB by ZnO and Se/ZnO.

electron hole recombination leading to enhanced photodegradation efficiency [57]. The improved photocatalytic performance could be attributed to the concentrations of oxygen vacancies, where it is high where the annealing temperature was low and decreases as the annealing temperature increases [53]. Similar results showing the consistence of MB photocatalytic degradation with the fiimi-order kinetic model were reported using different nanomaterials such as TiO_2 [58], $SrFe_{12}O_{19}$ [59], ZrC [60], and $ZnO/NiFe_2O_4$ [61]. The performance of the Se/ZnO NPs reported in this work is relatively better than the Se-doped samples used to degrade that could achieve only 50 % of the trypan blue dye in 2.5 h for 60 mg/100 mL [8].

3.9 Mechanism of Photocatalysis

Under UV light illumination with an energy equal to or greater than the band gap for photocatalyst, electrons are excited and are get promoted from VB to CB of ZnO or Se/ZnO leaving behind positive holes (h^+) [62, 63]. The strong oxidative species $O_2^{-\bullet}$ created from the electrons and O_2 reaction do combine with h^+ from solution to

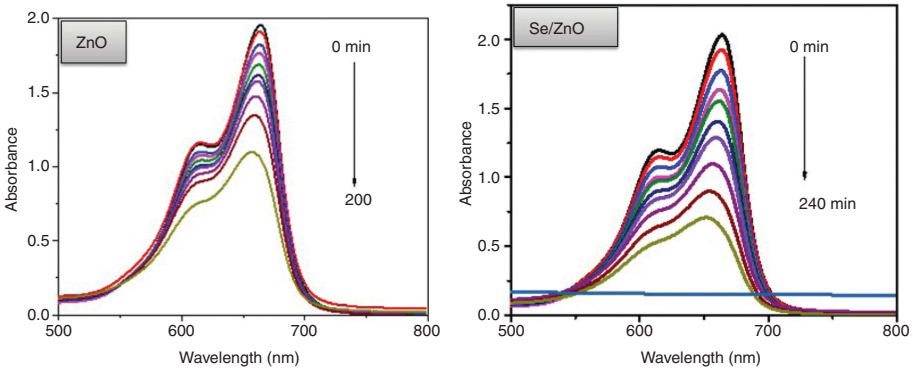

Figure 10: MB absorbance at different time intervals under UV irradiation.

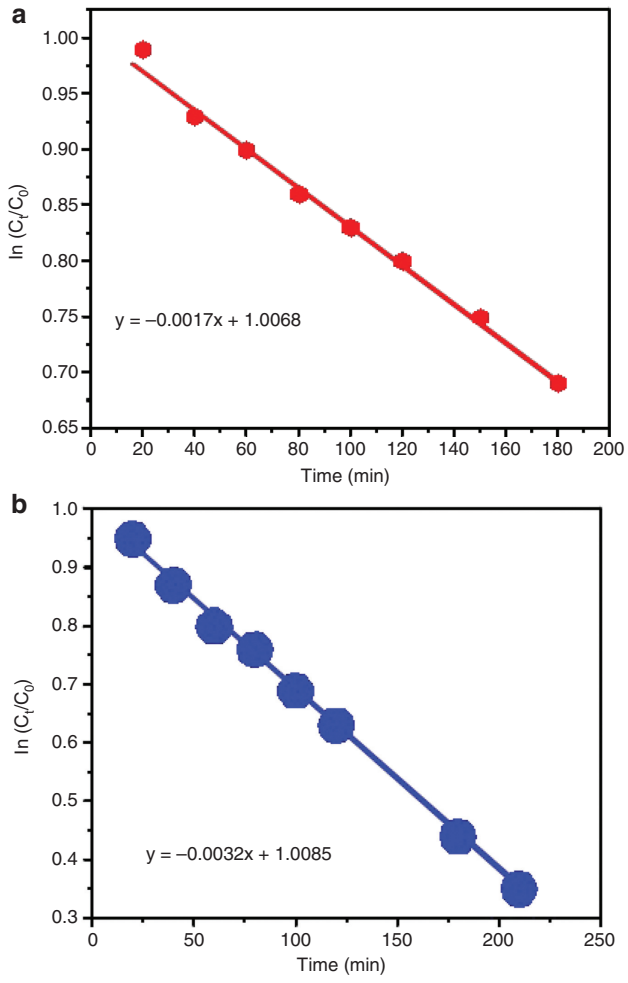

Figure 12: (a) Pseudo–first-order kinetics for MB photodegradation by ZnO. (b) Pseudo–first-order kinetics for MB photodegradation by Se/ZnO.

produce the peroxide H_2O_2 ($O_2 + 2\,h^+ + 2e^- \longrightarrow H_2O_2$) that undertakes series of reactions with electron to give the active $^{\cdot}OH$ radicals ($H_2O_2 + e^- \longrightarrow OH^- + {}^{\cdot}OH$). Also $^{\cdot}OH$ can be formed due to the reaction of the h^+ with surface adsorbed H_2O [64]. The photodegradation process can take place by the successive attacks on the organic dye by $^{\cdot}OH$ radicals ($R + {}^{\cdot}OH \longrightarrow R'' + H_2O$) or h^+ ($R + h^+ \longrightarrow R^{\cdot+} \longrightarrow$ degradation products) [65]. The CB edge potential (E_{CB}) and VB edge potential (E_{VB}) of ZnO and Se/ZnO can be calculated using the empirical formulae [66]:

$$E_{CB} = X - E_e - 0.5E_g \quad (16)$$

$$E_{VB} = X - E_e + 0.5E_g \quad (17)$$

where Eg is the band gap energy of the semiconductor, X is the electronegativity of the semiconductor (5.79 eV for ZnO). E_e is the energy of free electrons on the hydrogen scale (~4.5 eV). The CB and VB edges of ZnO were

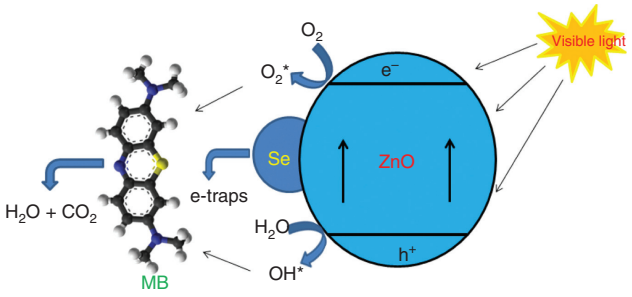

Figure 13: Degradation scheme.

−0.31 and 2.89 eV, and those of Se/ZnO were −0.29 and 2.87 eV, respectively. The electrons that get accumulated in the CB of ZnO can get transferred to the oxygen adsorbed onto the photocatalyst surface as the CB edge potential of ZnO (−0.31 eV vs. NHE) and Se/ZnO (−0.29 eV vs. NHE) [63] is more negative than the standard redox potential of ($O_2/O_2^{\cdot-}$) (−0.2 eV vs. NHE) [14, 67, 68] and therefore can reduce the O_2 to generate the $O_2^{\cdot-}$. In addition, the VB edge potential of ZnO (2.89 eV vs. NHE) and Se/ZnO (2.87 eV vs. NHE) was more positive than the standard redox potential of EH (OH/OH) = 1.99 eV (vs. NHE) [48], suggesting that the generated holes in the VB of ZnO and Se/ZnO can oxidise OH or H_2O to form $OH^{\cdot}$. Thus, the holes can undergo series of reactions to generate the highly reactive $OH^{\cdot}$ providing a constant flux of surface $OH^{\cdot}$ radicals [69] that can react with the organic dye. Figure 13 illustrates a diagrammatic representation for degradation process.

4 Conclusion

In summary, the synthesis of pure ZnO and Se/ZnO NPs was meritoriously achieved. The ZnO and Se/ZnO NPs were characterised using XRD, where the average crystallite size of obtained ZnO NPs ranges from 24 to 33 nm. A reduction in crystallite size of ZnO was observed when doping with Se as indicated by XRD data and imaging techniques (SEM and TEM) as well. The average c/a ratio was consistent with the values for the hexagonal Wurtzite structure of ZnO demonstrating that the nanostructures still retain the ZnO assembly. UV light–stimulated MB photodegradation using the target NPs was investigated where the outcomes have indicated a better performance of the doped sample. This study demonstrates that Se doping of ZnO greatly enhances the photodegradation performance of the nanomaterials toward organic dyes. The enhanced photodegradation efficiency of the Se/ZnO NPs can be related to its decreased band gap energy as revealed by the DRS investigation along with the large surface area available for the dye adsorption. The calculated valence

and CB edge positions indicated that the MB photodegradation could be attributed to the $OH^{\bullet}$ radicals generated by the h^+ reaction with the OH^- or H_2O adsorbed on the photocatalyst surface.

References

[1] Z. L. Wang, ACS Nano **2**, 1987 (2008).
[2] C.-T. Lee, Materials **3**, 2218 (2010).
[3] S. Shi, Y. Yang, J. Xu, L. Li, X. Zhang, et al., J. Alloy. Compd. **576**, 59 (2013).
[4] T. Minami, H. Nanto, and S. Takata, Jpn. J. Appl. Phys. **24**, L781 (1985).
[5] V. V. Khomyak, O. M. Slyotov, and S. M. Chupyra, Appl. Optics **53**, B110 (2014).
[6] R. Elsalamony, Res. Rev. J. Mater. Sci. **4**, 26 (2016).
[7] S. Chaudhary, A. Umar, and S. Mehta, Prog. Mater. Sci. **83**, 270 (2016).
[8] B. P. Nenavathu, A. V. R. Krishna Rao, A. Goyal, A. Kapoor, and R. Kumar Dutta, Appl. Catal. A-Gen. **459**, 106 (2013).
[9] R. K. Dutta, B. P. Nenavathu, and S. Talukdar, Colloid. Surface. B **114**, 218 (2014).
[10] V. Khomyak, M. Slyotov, I. Shtepliuk, O. Slyotov, and V. Kosolovskiy, Acta Phys. Pol. A **122**, 1039 (2012).
[11] T. T. Tan, M. Zaw, D. Beydoun, and R. Amal, J. Nanopart. Res. **4**, 541 (2002).
[12] M. Perez, F. Torrades, X. Domenech, and J. Peral, Water Res. **36**, 2703 (2002).
[13] M. M. Khin, A. S. Nair, V. J. Babu, R. Murugana, and S. Ramakrishna, Energ. Environ. Sci. **5**, 8075 (2012).
[14] S. Talukdar and R. K. Dutta, RSC Adv. **6**, 928 (2016).
[15] G. Pliego, J. A. Zazo, J. A. Casas, and J. J. Rodriguez, J. Hazard. Mater. **252**, 180 (2013).
[16] J. Paul, K. P. Rawat, K. S. S. Sarma, and S. Sabharwal, Appl. Radiat. Isotopes **69**, 982 (2011).
[17] B. C. Lippens and J. de Boer, J. Catal. **4**, 319 (1965).
[18] A. Meng, J. Xing, Z. Li, and Q. Li, ACS Appl. Mater. Inter. **7**, 27449 (2015).
[19] A. K. Zak, W. H. Abd Majid, M. E. Abrishami, and R. Yousefi, Solid State Sci. **13**, 251 (2011).
[20] B. E. Langner, in: Ullmann's Encyclopedia of Industrial Chemistry 2000. Print ISBN: 9783527303854, Online ISBN: 9783527306732, DOI: 10.1002/14356007.
[21] A. Patterson, Phys. Rev. **56**, 978 (1939).
[22] L. Damonte, L. Mendoza-Zélis, B. M. Soucase, and M. A. Hernández-Fenollosa, Powder Technol. **148**, 15 (2004).
[23] C. Barrett and T. Massalski, Structure of Metals, 3 rd ed., Pergamon Press, Oxford 1980.
[24] U. Seetawan, S. Jugsujinda, T. Seetawan, A. Ratchasin, C. Euvananont, et al., Mater. Sci. Appl. **2**, 1302 (2011).
[25] G. Srinivasan, R. R. Kumar, and J. Kumar, J. Sol-Gel Sci. Techn. **43**, 171 (2007).
[26] D. Aryanto, W. N. Jannah, Masturi, T. Sudiro, A. S. Wismogroho, et al., J. Phys. Conf. Ser. IOP Publishing, Jakarta, Indonesia 2017.
[27] M. Geetha, H. Nagabhushana, and H. Shivananjaiah, J. Sci. Adv. Mater. Devices **1**, 301 (2016).
[28] M. Thirumoorthi and J. T. J. Prakash, Superlattice. Microst. **85**, 237 (2015).
[29] K. V. Rao and C. Sunandana, J. Mater. Sci. **43**, 146 (2008).
[30] P. Bindu and S. Thomas, J. Theor. Appl. Phys. **8**, 123 (2014).
[31] A. Gupta, V. Singhal, and O. Pandey, J. Alloy. Compd. **736**, 306 (2018).
[32] T. Ungár, J. Mater. Sci. **42**, 1584 (2007).
[33] T. Pandiyarajan and B. Karthikeyan, J. Nanopart. Res. **14**, 647 (2012).
[34] R. Jacob and J. Isac, Int. J. Chem. Stud. **2**, 12 (2015).
[35] S. Amirkhanlou, M. Ketabchi, and N. Parvin, Mater. Lett. **86**, 122 (2012).
[36] M. Arshad, A. Azam, A. S. Ahmed, S. Mollah, and A. H. Naqvi, J. Alloy. Compd. **509**, 8378 (2011).
[37] S. Muthukumaran and R. Gopalakrishnan, Opt. Mater. **34**, 1946 (2012).
[38] N. H. Hashim, S. Subramani, M. Devarajan, and A. R. Ibrahim, J. Mater. Sci. Mater. Electr. **27**, 3520 (2016).
[39] Z. Quan, D. Li, B. Sebo, W. Liu, S. Guo, et al., Appl. Surf. Sci. **256**, 3669 (2010).
[40] G. G. Gospodinov, Thermochim. Acta **77**, 439 (1984).
[41] I. Korneeva and A. Novoselova, Zh. Neorg. Khim. **4**, 2220 (1959).
[42] C. Clarkson and R. Bustin, Fuel, **78**, 1333 (1999).
[43] S. Kuśnieruk, J. Wojnarowicz, A. Chodara, T. Chudoba, S. Gierlotka, et al., Beilstein J. Nanotech. **7**, 1586 (2016).
[44] K. Elen, A. Kelchtermans, H. Van den Rul, R. Peeters, J. Mullens, et al., J. Nanomater. **2011**, 18 (2011).
[45] T. C. DeVore and V. Harrisonburg, Thermal Decomposition of Zinc Oxalate Dihydrate and Zinc Ammine Oxalate Dihydrate 2005.
[46] S. Hosseini, I. A. Sarsari, P. Kameli, and H. Salamati, J. Alloy. Compd. **640**, 408 (2015).
[47] M. Mittal, M. Sharma, and O. Pandey, Sol. Energy **110**, 386 (2014).
[48] H. Lu, L. Liao, J. Li, D. Wang, H. He, et al., J. Phys. Chem. B **110**, 23211 (2006).
[49] I. Shalish, H. Temkin, and V. Narayanamurti, Phys. Rev. B **69**, 245401 (2004).
[50] J. Tauc, Mater. Res. Bull. **3**, 37 (1968).
[51] A. Gupta and O. Pandey, Sol. Energy **163**, 167 (2018).
[52] D. Mocatta, G. Cohen, J. Schattner, O. Millo, E. Rabani, et al., Science **332**, 77 (2011).
[53] J. Wang, Z. Wang, B. Huang, Y. Ma, Y. Liu, et al., ACS Appl. Mater. Inter. **4**, 4024 (2012).
[54] Z. Fang, S. Weng, X. Ye, W. Feng, Z. Zheng, et al., ACS Appl. Mater. Inter. **7**, 13915 (2015).
[55] S. Kappadan, T. Gebreab, S. Thomas, and N. Kalarikkal, Mat. Sci. Semicon. Proc. **51**, 42 (2016).
[56] K. Sopajaree, S. A. Qasim, S. Basak, and K. Rajeshwar, J. Appl. Electrochem. **29**, 533 (1999).
[57] W. Liu, Y. Shang, A. Zhu, P. Tan, Y. Liu, et al., J. Mater. Chem. A **5**, 12542 (2017).
[58] T. Zhang, T. Oyama, A. Aoshima, H. Hidaka, J. Zhao, et al., J. Photoch. Photobio. A **140**, 163 (2001).
[59] D. D. Mishra and G. Tan, J. Phys. Chem. Solids **123**, 157 (2018).
[60] A. S. Vig, A. Gupta, and O. Pandey, Adv. Powder Technol. **29**, 2231 (2018).
[61] J. Adeleke, T. Theivasanthi, M. Thiruppathi, M. Swaminathan, T. Akomolafe, et al., Appl. Surf. Sci. **455**, 195 (2018).

[62] J. Wang, H. Shen, X. Dai, C. Li, W. Shi, et al., Mater. Technol. **33**, 421 (2018).
[63] D. Hidalgo, S. Bocchini, M. Fontana, G. Saraccob, and S. Hernández, RSC Adv. **5**, 49429 (2015).
[64] K. K. Chattopadhyay, S. Maiti, S. Pal, Cryst. Eng. Comm. **17**, 9264 (2015).
[65] A. Houas, H. Lachheb, M. Ksibi, E. Elaloui, C. Guillard, et al., Appl. Catal. B-Environmental **31**, 145 (2001).
[66] R. Saravanan, V. K. Gupta, E. Mosquera, and F. Gracia, J. Mol. Liq. **198**, 409 (2014).
[67] X. Fu, W. Tang, L. Ji, and S. Chen, Chem. Eng. J. **180**, 170 (2012).
[68] Z. Li, Z. Xie, Y. Zhang, L. Wu, X. Wang, et al., J. Phys. Chem. C **111**, 18348 (2007).
[69] W. Liu, M. Wang, C. Xu, and S. Chen, Chem. Eng. J. **209**, 386 (2012).